ORGANIC CHEMISTRY

FRONTIERS

RESEARCH ARTICLE

Check for updates

Z-shaped polycyclic aromatic hydrocarbons with embedded five-membered rings and their application in organic thin-film transistors†‡

Sven M. Elbert,[a] Evelin Bolgert,[a] Owen T. A. Paine,[a] Farhad Ghalami,[b]
Wen-Shan Zhang, [ID] [a] Ute Zschieschang,[c] Frank Rominger,[a] Dennis Popp,[a]
Hagen Klauk, [ID] [c] Marcus Elstner [ID] [b] and Michael Mastalerz [ID] *[a]

Z-shaped polycyclic hydrocarbons with embedded five-membered rings as well as their diaza-analogues have been synthesized. Soluble congeners were obtained by the introduction of mesityl substituents and studied by cyclo- as well as differential pulse voltammetry revealing an amphoteric redox behavior. Unsubstituted congeners showed close π-stacking in single crystal X-ray diffraction analyses and thus promising characteristics for the application as semiconducting materials in p-channel thin-film transistors (TFTs). The hole transport characteristics of the corresponding devices were investigated by GIWAXS.

Introduction

Polycyclic aromatic hydrocarbons with fused five-membered rings (also named cyclopenta-fused or short cp-PAHs) are a subclass of non-alternant PAHs with unique electronic and photophysical properties.[1,2] cp-PAHs often represent cut-outs of fullerenes such as C_{60} or C_{70} and have a high electron affinity.[3–8] Thus, cp-PAHs found application as semiconductors in electronic devices.[9–11] For example, the dibenzo [a,m]rubicene (Fig. 1),[12] a cut-out of C_{70} with two five-membered rings in the aromatic backbone was used as p-type organic semiconductor with a field effect mobility of 1.0 cm^2 V^{-1} s^{-1} in thin-film transistors (TFTs).[13–15] Another cp-PAH with two five-membered rings, a derivative of acenaphto[1,2-k] fluoranthene[16] (Fig. 1), was used as a green emissive dye in organic light-emitting diodes (OLEDs).[17]

Besides cp-PAHs, zethrenes are another class of Z-shaped PAHs with exceptional properties.[18,19] They have biradical character with indices up to $\gamma_0 = 0.58$. The γ_0-values were tuned by benzannulation as shown in the cases of the 1,2:9,10-, and the 5,6:13,14-dibenzoheptazethrenes (short: DBHZ; Fig. 1).[20] Furthermore, for organic field effect transistors (OFETs) based on single crystals of a DBHZ, a hole mobility up to 0.15 cm^2 V^{-1} s^{-1} was obtained.[21]

Rubicenes[14,22–25] and some of their extended congeners are rare examples combining both, a molecular Z-shape with
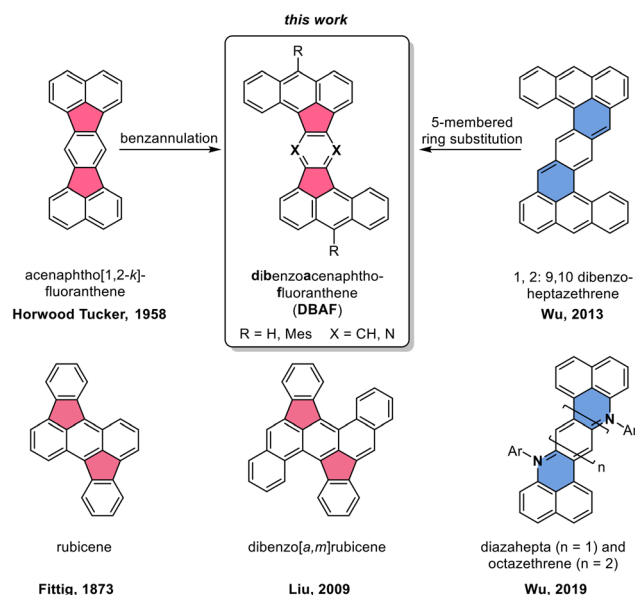

Fig. 1 Top: Molecular structures of acenaphtho[1,2-k]fluoranthene[16] (left) and 1,2:9,10-dibenzoheptazethrene[20] (right) and the hypothetical structural relationship to the dibenzoacenaphthofluoranthenes (DBAFs; middle). Bottom: Structure of rubicene (left),[22,23] dibenzo[a,m]rubicene[12] and diaza zethrenes.[27]

[a]*Institute of Organic Chemistry, Ruprecht-Karls-Universtity Heidelberg, Im Neuenheimer Feld 270, 69120 Heidelberg, Germany.
E-mail: michael.mastalerz@oci.uni-heidelberg.de*
[b]*Institute of Physical Chemistry and Theoretical Chemical Chemistry, Karlsruhe Institute of Technology, Kaiserstraße 12, D-76131 Karlsruhe, Germany*
[c]*Max Planck Institute for Solid State Research, Heisenbergstr. 1, 70569 Stuttgart, Germany*

This journal is © the Partner Organisations 2024

embedded five-membered rings which is created by a phenyl–anthracenyl–phenyl scaffold (Fig. 1).[26] We envisioned to extend the portfolio of PAHs (or cp-PAHs) in this respect by a series of compounds which can be understood either as benzannulated acenaphtofluoranthenes or as 1,2:9,10-dibenzoheptazethrenes with two six-membered rings formally substituted by five-membered ones (shown in blue and red in Fig. 1). Therefore, these compounds are named dibenzoacenaphthofluoranthenes, abbreviated as DBAFs. The DBAFs have an "inverted" anthracenyl-phenyl-anthracenyl scaffold in comparison to rubicenes (Fig. 1).[26]

By simple modifications of the molecular precursors, nitrogen substituted analogues (the DBAF-N₂s) are accessible to investigate the influence of nitrogen substitution on the compounds' properties which was for example realized for diazahepta and octazethrenes[27–29] (Fig. 1) and is generally rare in the field of cp-PAHs.[30,31]

Results and discussion

The Z-shaped five-membered ring containing PAHs were obtained by Suzuki–Miyaura cross-coupling reactions followed by palladium-catalysed arylations under C–H activation starting from dichlorodibromobenzene **1**[32] or -pyrazine **2**[33] (Scheme 1). The cross-coupling of **1** or **2** with 9-anthracenylboronic acid **3** gave the corresponding products **5** and **6** in 80% and 56% yield respectively. The mesityl-substituted congeners **7** and **8** were obtained from **1** and **2** with 10-mesitylanthracenyl boronic pinacol ester **4** in 34% and 68% yield. Compounds **5–8** were fully characterized by NMR as well as IR spectroscopy, mass spectrometry and their constitution was unambiguously proven by single crystal X-ray diffraction (SCXRD; for details see ESI‡).

Subjecting the four dichlorinated precursors **5–8** to typical conditions for arylations under C–H-activation (PdCl₂(PCy₃)₂, DBU, DMAc, 200 °C, 48 h)[34–41] gave after sublimation unsubstituted **DBAF** in 96% and **DBAF-N₂** in 55% yield as well as the

mesityl substituted **mes-DBAF** in 33% and **mes-DBAF-N₂** in 69% after column chromatography (Scheme 1). The parent **DBAF** and **DBAF-N₂** are poorly soluble in common organic solvents at room temperature and NMR spectroscopy had to be performed in *ortho*-dichlorobenzene-d₄ at elevated temperatures (323 K; see ESI‡). The successful pentannulations have been proven by 1D- and 2D-NMR spectroscopy as well as mass spectrometry (see ESI‡) and by SCXRD analyses (see discussion below).

The optical properties of the DBAF series were investigated by UV/vis- as well as fluorescence spectroscopy in *o*DCB (**DBAF** and **DBAF-N₂**) or dichloromethane (**mes-DBAF** and **mes-DBAF-N₂**) (Fig. 2 and Table 1). **DBAF** and **DBAF-N₂** were only soluble in *o*DCB after heating and ultrasonication. **DBAF** shows an intensive absorption maximum at λ_{abs} = 349 nm and additional low energy absorption maxima at λ_{abs} = 461, 491, 518 and 550 nm. A red emission can be detected by bare eye, which corresponds to a maximum at λ_{em} = 572 nm and a shoulder at $\lambda_{em} \sim$ 620 nm with a Stokes shift of $\tilde{\nu}$ = 699 cm⁻¹ and a photoluminescence quantum yield of φ = 21%.

mes-DBAF shows similar spectroscopic properties as its non-mesitylated analogue with a high intensity absorption band at λ_{abs} = 350 nm (**DBAF**: 349 nm) and again poorly resolved maxima at λ_{abs} = 460, 493, 526 and 561 nm and a slightly red-shifted emission with λ_{em} = 588 nm (**DBAF**: 572 nm) leading to a larger Stokes shift of $\tilde{\nu}$ = 819 cm⁻¹ (φ = 20%, Table 1).

DBAF-N₂ shows two maxima at λ_{abs} = 379 and 399 nm and a less resolved pattern of overlapping adsorption maxima with a most red-shifted maximum at λ_{abs} = 519 nm with a shoulder at λ_{abs} = 555 nm. The corresponding emission maximum is found at λ_{em} = 577 nm with a shoulder at λ_{em} = 621 nm and a
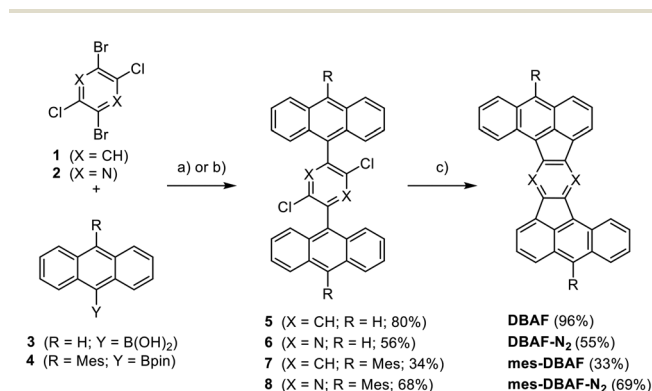
Scheme 1 Synthesis of **DBAF**, **DBAF-N₂**, **mes-DBAF** and **mes-DBAF-N₂** from dibromodichlorobenzene **1** and dibromodichloropyrazine **2**. (a) For **5** and **7**: Pd(OAc)₂ (2.5–3 mol%), SPhos (5–6 mol%), K₂CO₃ aq. (1 M), THF, 85 °C 16 h; for **6** and **8**: (b) Pd(dppf)Cl₂ (10 mol%), K₂CO₃ (1 M), THF, 85 °C, 16 h, (c) PdCl₂(PCy₃)₂, DBU, DMAc, 200 °C, 16 h.
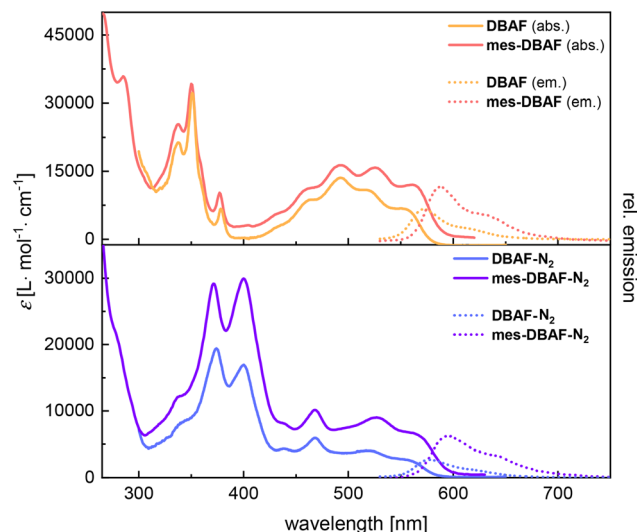
Fig. 2 UV/vis absorption (solid lines) and fluorescence (dashed lines) spectra of **DBAF** (red) and **mes-DBAF** (orange) (top) and **DBAF-N₂** (blue) and **mes-DBAF-N₂** (violet) (bottom), measured in *o*-DCB (**DBAF** and **DBAF-N₂**) or CH₂Cl₂ (**mes-DBAF**) and **mes-DBAF-N₂** at room temperature.

This journal is © the Partner Organisations 2024

Org. Chem. Front., 2024, **11**, 5340–5349 | **5341**

Table 1 Optical and electronic properties of the DBAF-series

Cmpd	$\lambda_{max}^{a,b}$ [nm]	λ_{onset}^{b} [nm]	$E_{gap,opt}^{c}$ [eV]	λ_{em}^{b} [nm]	$\tilde{\nu}_{Stokes}^{b}$ [cm^{-1}]	$PLQY^{b}$ [%]	$E_{IP,CV}^{d}$ [eV]	$E_{EA,CV}^{d}$ [eV]	$E_{gap,CV}$ [eV]	$E_{HOMO,DFT}^{e}$ [eV]	$E_{LUMO,DFT}^{e}$ [eV]	$E_{Diff,DFT}^{e}$ [eV]
DBAF	550	581	2.1	572	699	21	—^{f}	—^{f}	—^{f}	−5.0	−2.4	2.6
DBAF-N$_2$	555	582	2.1	577	687	5	—^{f}	—^{f}	—^{f}	−5.2	−2.6	2.6
mes-DBAF	561	589	2.1	588	819	20	−5.3	−3.0	2.3	−4.9	−2.4	2.6
mes-DBAF-N$_2$	561	592	2.1	593	961	29	−5.6	−3.2	2.4	−5.1	−2.5	2.6

^{a} Most-red-shifted absorption maximum. ^{b} **DBAF** and **DBAF-N$_2$** were measured in o-DCB at room temperature; **mes-DBAF** and **mes-DBAF-N$_2$** were measured in CH$_2$Cl$_2$ at room temperature. ^{c} Estimated from the corresponding λ_{onset} by $E_{gap,opt} = 1240/\lambda_{onset}$. ^{d} Cyclic voltammograms (CV) of **mes-DBAF** and **mes-DBAF-N$_2$** in dichloromethane (c = 1 mM) using [Bu$_4$N][PF$_6$] (0.1 M) as electrolyte. CV scan speed 100 mV s^{-1}. $E_{IP,CV} = -(E_{1/2}^{Ox} + 4.8$ eV$)$; $E_{EA,CV} = -(E_{1/2}^{red} + 4.8$ eV$)$. ^{e} Calculated at the u-B3LYP/6-31G(d,p) level of theory. ^{f} Not determined due to solubility issues.
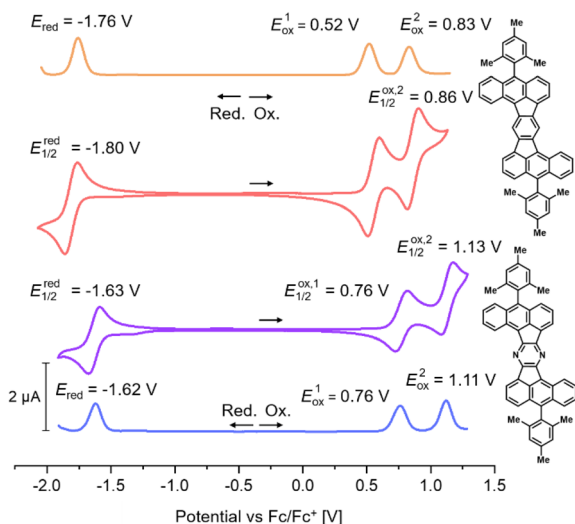
Stokes shift of $\tilde{\nu}$ = 687 cm^{-1} with φ = 5% (Table 1). Similarly, as for **mes-DBAF** and **DBAF** the spectral differences of **mes-DBAF-N$_2$** and **DBAF-N$_2$** are negligible (Fig. 2 and Table 1), indicating that the mesityl groups change the solubility without significantly influencing the optoelectronic properties of the molecular scaffolds.

As already mentioned, **DBAF** and **DBAF-N$_2$** are poorly soluble in organic solvents so that decent cyclovoltammograms could not be recorded. Therefore, only the mesitylated derivatives **mes-DBAF** and **mes-DBAF-N$_2$** have been investigated by cyclic as well as differential pulse voltammetry revealing an amphoteric redox behaviour in both cases (Fig. 3). Two reversible oxidations can be found for **mes-DBAF** at E_{Ox}^1 = 0.52 V and E_{Ox}^2 = 0.83 V as determined by DPV (CV: $E_{1/2}^{Ox,1}$ = 0.56 V und $E_{1/2}^{Ox,2}$ = 0.86 V) and one reversible reduction was detected at E_{red} = −1.76 V (CV: $E_{1/2}^{red}$ = −1.80 V). For **mes-DBAF-N$_2$** the corresponding oxidation waves appear at approx.

Fig. 3 Cyclic voltammograms (CV) and differential pulse voltammograms (DPV) of **mes-DBAF** (top) and **mes-DBAF-N$_2$** (bottom) in dichloromethane (c = 1 mM) using [Bu$_4$N][PF$_6$] (0.1 M) as electrolyte. CV scan speed 100 mV s^{-1}; DPV: step size of 0.005 V, a modulation amplitude of 0.025 V a modulation time of 0.05 s and an interval time of 0.5 s.

0.2–0.3 V higher potentials with E_{Ox}^1 = 0.76 V and E_{Ox}^2 = 1.11 V (CV: $E_{1/2}^{Ox,1}$ = 0.76 V und $E_{1/2}^{Ox,2}$ = 1.13 V). The reduction is shifted by 0.14 V to higher potentials with E_{red} = −1.62 V (CV: $E_{1/2}^{red}$ = 1.63 V) indicating the electrochemical stabilization of PAHs by nitrogen substitution.[42–44] This is further displayed in the differences of the corresponding ionization potentials (**mes-DBAF**: IP = −5.32 eV; **mes-DBAF-N$_2$**: IP = −5.56 eV) as well as electron affinities (**mes-DBAF**: EA = −3.04 eV; **mes-DBAF-N$_2$**: EA = −3.18 eV) derived from this data. By UV/vis spectrsocopy it was demonstrated that the mesityl substituents, which are oriented orthogonal to the π backbone, do not significantly influence these electronically. Therefore, it is assumed that the redox behaviour of **DBAF** and **DBAF-N$_2$** are comparable to **mes-DBAF** and **mes-DBAF-N$_2$**. By DFT calculations (u-B3LYP/6-31G(d,p); Fig. 4 and Table 1) a 0.19 eV lower HOMO energy of **mes-DBAF-N$_2$** (E_{HOMO} = −5.12 eV) in comparison to **mes-DBAF** (E_{HOMO} = −4.93 eV) is found as well as a 0.14 eV lower LUMO energy (**mes-DBAF-N2**: E_{LUMO} = −2.52 eV; **mes-DBAF**: E_{LUMO} = −2.38 eV), which corroborates with the trend found by CV.
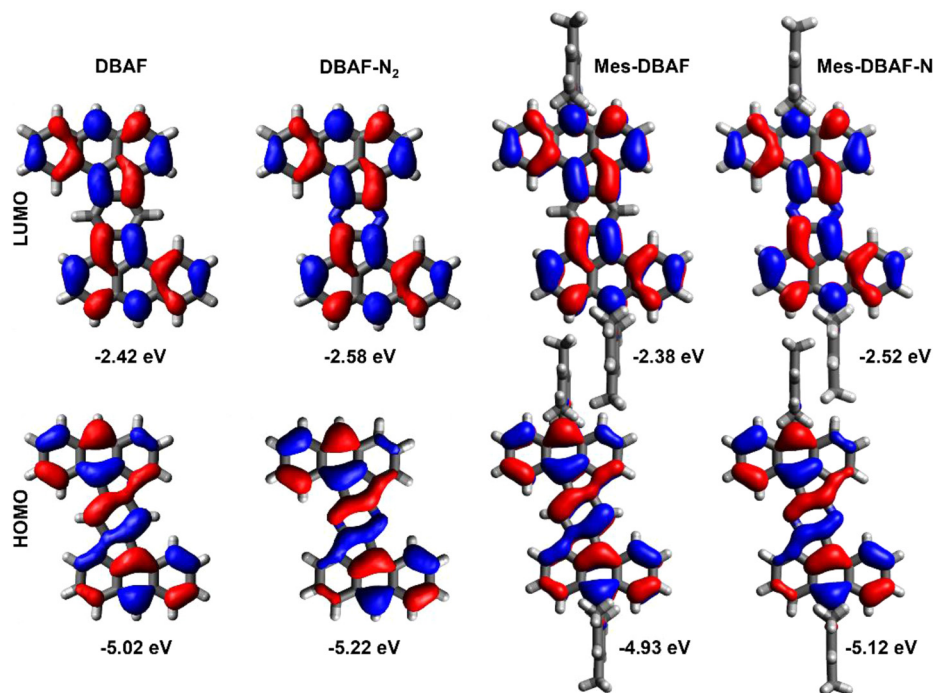
Again, the mesityl substituents seem to only have a small influence to the energy levels with the HOMOs being lowered by only 0.09–0.1 eV and the LUMOs by only 0.04–0.06 eV for **DBAF** and **DBAF-N$_2$** in comparison to their mesitylated congeners (Fig. 4 and Table 1) and the distribution of frontier molecular orbital coefficients are nearly the same for all four compounds (Fig. 4).

By thermal crystallization from *ortho*-dichlorobenzene as well as by sublimation isomorphic single crystals of **DBAF** suitable for SCXRD were obtained. **DBAF** crystallizes in the monoclinic space group $P2_1/n$ with Z = 2. The crystalline packing is dominated by slipped π-stacked molecular columns (Fig. 5b and c) with a spacing of $d_{\pi-\pi}$ = 3.33 Å propagating along the crystallographic a-axis. Edge-to-face π stacking with $d_{C-H\cdots\pi}$ = 2.70 Å and an angle of the π-systems of θ = 51.8° (Fig. 5c) leads to a herringbone like motif (Fig. 5d). Suitable crystals of **DBAF-N$_2$** have also been obtained by sublimation. **DBAF-N$_2$** also crystallized in the $P2_1/n$ space group and again slipped π-stacked columns can be found, here with a slightly larger distance of $d_{\pi-\pi}$ = 3.40 Å but with a larger overlap of two adjacent π systems (compare Fig. 5b and f). Similar edge-to-face π stacking is found but with a larger angle of θ = 73.1° and a larger

5342 | *Org. Chem. Front.*, 2024, **11**, 5340–5349

This journal is © the Partner Organisations 2024

Fig. 4 DFT-calculated frontier molecular orbitals on the u-B3LYP/6-31G(d,p) level of theory (LUMOs top; HOMOs bottom) of (from left to right) **DBAF**, **DBAF-N₂**, **mes-DBAF** and **mes-DBAF-N₂** with the calculated energy levels.

distance between adjacent molecules ($d_{C–H\cdots\pi}$ = 2.87 Å), leading to a herringbone type packing as well (Fig. 5g and h). Single-crystals of **mes-DBAF** were obtained by slow evaporation of a chloroform solution and crystallized in the monoclinic space group $P2_1/n$ with Z = 2. This time with one enclathrated disordered molecule of chloroform per **mes-DBAF** (Fig. 5). Due to the almost perpendicular oriented (87.6°) mesityl groups, no direct π stacking of the DBAF central backbone is found (Fig. 5i). Instead, the crystalline packing is dominated by C–H⋯π-interactions of the *para*-methyl-group of a mesityl substituent with the central benzene ring of the DBAF backbone ($d_{C–H\cdots\pi}$ = 2.34 Å) leading to a loose herringbone-like arrangement with chloroform molecules in its voids (Fig. 5j–l). Crystals of **mes-DBAF-N₂** were obtained by vapor phase diffusion of n-hexane into a saturated chloroform solution. **mes-DBAF-N₂** also crystallized in the monoclinic space group $P2_1/n$ with Z = 2. In contrast to **mes-DBAF, mes-DBAF-N₂** shows linear columns of face-to-face π stacks along the crystallographic *a*-axis (Fig. 5n and p). Within these stacks two symmetrically independent molecules with unparallel π-planes and a shortest distance of $d_{\pi–\pi}$ = 3.22 Å are found in a rare twisted offset[45–47] with an angle of ~32° between the central molecular axes to maximize orbital overlaps by avoiding the steric repulsion of the mesityl groups. The columns themselves interact with each other by dispersion interactions between the methyl groups of the mesityl substituents.

Charge transfer integrals (t) between the molecules as well as intrinsic charge carrier mobilities (hole and electron) were calculated *via* fragment based non-adiabatic molecular dynamic simulations (for a detailed description of the method see ESI‡).[48,49] Only hole transport properties will be discussed (calculated electron transport properties can be found in the ESI‡), due to the fact, that the experimentally determined electron affinities of EA = −3.04 to −3.18 eV exclude a potential use in n-type semiconducting devices due to a mismatch with the work functions of commonly used electrode materials such as gold.[50] The hole transfer integral of **DBAF** along the axis of the face-to-face stacking was calculated using the non-self-consistent density functional tight binding (DFTB) method with special parameter set[51] to be $t_{\parallel,h}$ = 20 ± 14 meV (Fig. 5d). In the direction of the edge-to-face stacking only small transfer integrals were found ($t_{\perp,h}$ = 1 ± 3 meV). The corresponding theoretical hole mobility of μ_h = 0.31 cm² V⁻¹ s⁻¹ calculated by the fewest switches surface hopping algorithm with implicit relaxation (FSSH-IR), where the reorganization energy is calculated by DFT with B3LYP functional and 6-31G(d,p) level of theory to be $\lambda_{h,\ B3LYP}$ = 153 meV indicates the potential use of **DBAF** in such devices. In the case of **DBAF-N₂** (Fig. 5h), a higher electronic coupling with transfer integrals of $t_{\parallel,h}$ = 70 ± 24 meV was found. The corresponding hole mobilities of μ_h = 14.41 cm² V⁻¹ s⁻¹ are based on a reorganization energy of $\lambda_{h,\ B3LYP}$ = 167 meV. The mesitylated congeners **mes-DBAF** and **mes-DBAF-N₂** showed either no or only negligible theoretical mobilities and have thus been excluded for device fabrication (see ESI‡ for further details).

Organic p-channel TFTs of **DBAF** gave hole mobilities of 1 × 10⁻⁴ to 1 × 10⁻³ cm² V⁻¹ s⁻¹ independent of the type of the substrate (silicon or flexible polyethylene naphthalate (PEN))
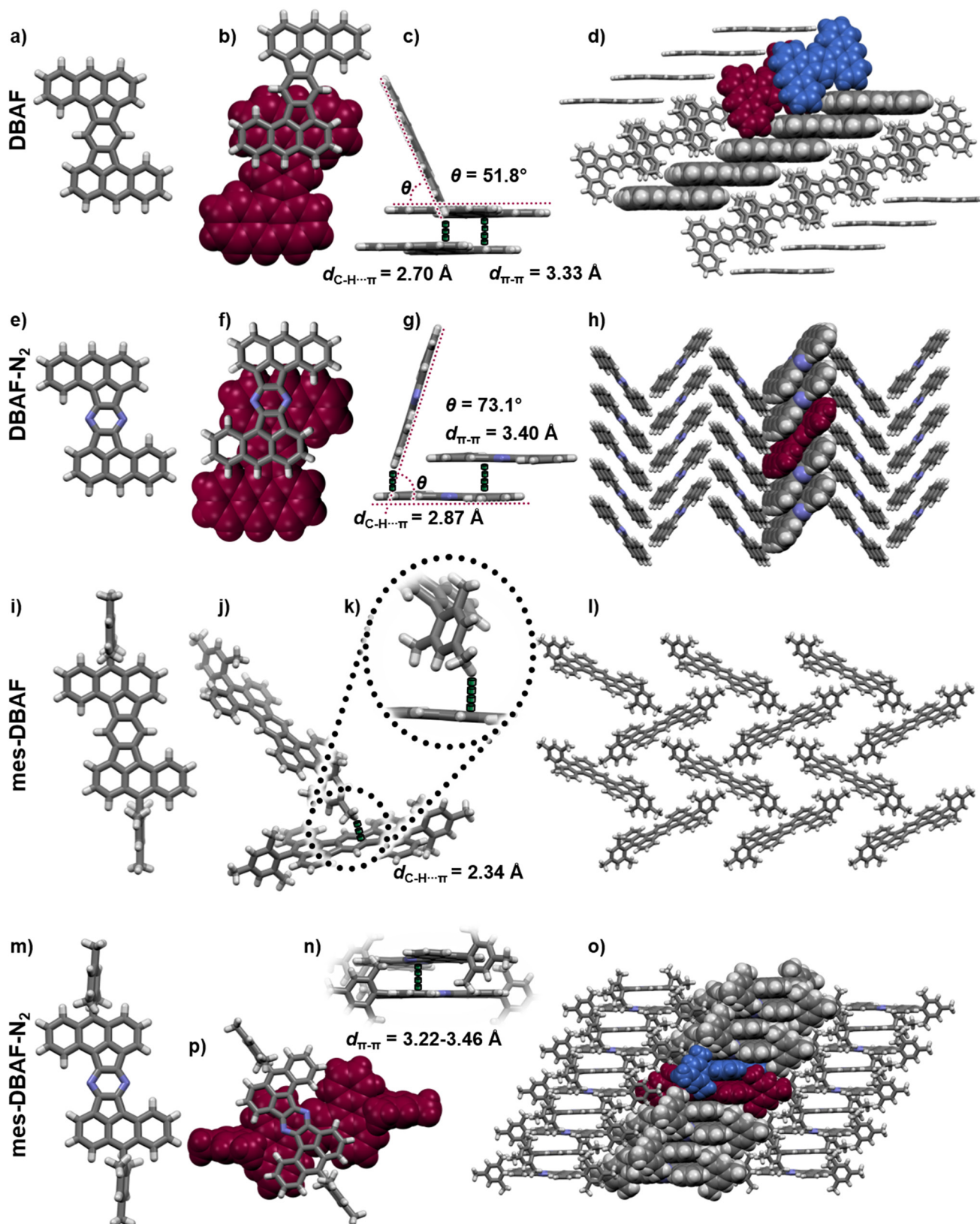
Fig. 5 Single crystal X-ray structures of **DBAF** (a–d), **DBAF-N$_2$** (e–h), **mes-DBAF** (i–l) and **mes-DBAF-N$_2$**. a, e, i and m: molecular structures. b, f and p: top-view on face-to-face π-stacked dimers. c, g and j: side-view on edge-to-face interactions. d, h, l and o: molecular packings. k: zoom-in on the C−H···π-interaction of **mes-DBAF**. n: side-view on the face-to-face π-stacked dimer of **mes-DBAF-N$_2$**.

5344 | *Org. Chem. Front.*, 2024, **11**, 5340–5349

This journal is © the Partner Organisations 2024

and the substrate temperature during the vacuum deposition of the semiconductor (60 or 80 °C) when using a pentadeca-fluoro-octadecylphosphonic acid self-assembled monolayer (F-SAM) as part of the gate dielectric.[52]

These mobilities significantly increased using an *n*-tetrade-cylphosphonic acid SAM (H-SAM) instead. In this case, mobilities of 0.08 up to 0.4 cm^2 V^{-1} s^{-1} have been obtained, again independent of the type of substrate and the substrate temperature during the semiconductor deposition. The best TFT performance was obtained on a PEN substrate using a substrate temperature of 80 °C during the semiconductor deposition (for details see ESI‡), with a mobility of $\mu_{h,exp}$ = 0.4 cm^2 V^{-1} s^{-1} (Fig. 6), which is in good agreement to the theoretical mobility discussed above ($\mu_{h,theo}$ = 0.31 cm^2 V^{-1} s^{-1}). Although **DBAF-N$_2$** showed even higher theoretical hole mobilities ($\mu_{h,theo}$ = 14.41 cm^2 V^{-1} s^{-1}, see discussion above), the mobilities obtained experimentally are much smaller, only 4×10^{-5} to 5×10^{-4} cm^2 V^{-1} s^{-1}, independent of the type of substrate, the type of SAM, and the substrate temperature during the semiconductor deposition. The calculated values represent the intrinsic mobility in the perfect crystalline structures of **DBAF** and **DBAF-N$_2$**, where no grain boundaries or other defects are present. However, in thin-films, such defects exist, and the thin-film structures may deviate from the ideal single-crystal form. Consequently, the calculated mobilities provide a useful estimation of how closely the deposited thin-films approximate a perfect single crystal. This can be inferred from the similarity of their charge-transport properties. The significant difference between the experimental and theoretical mobilities suggests that the deposited **DBAF-N$_2$** structure deviates considerably from the perfect crystal structure.

To better understand the measured TFT characteristics (schematic device structure shown in Fig. 7a), grazing-incidence wide-angle X-ray scattering (GIWAXS) was employed. The critical angles (α_c) of **DBAF** and **DBAF-N$_2$** are estimated at 0.17° and 0.18°, respectively.[53] Therefore, the incident angle (α_i) of the incoming X-ray was set at 0.3° ($\alpha_i > \alpha_c$) in order to probe microstructures of the deeper-lying organic/SAM/inorganic interface, rather than those from the topmost surface. Though the AFM and SEM investigations reveal the polycrystallinity of the thin-films with non-specific orientations, the small grain size (~0.1–0.5 μm) makes the in-plane information difficult or impossible to be detected by GIWAXS. Instead, we obtain the strong out-of-plane signals and are thus able to analyze the interface configurations. Two sets of out-of-plane signals have been observed. As exemplified in Fig. 7c and d, the lower one at ~21 Å stems from the self-assembled monolayer that is part of the gate dielectric, while the upper one at ~10 Å belongs to the organic semiconductor thin-films. Specifically, for **DBAF**, the reflex at 9.99 Å is assigned to the (001) plane (10.5 Å calculated from the signal crystal data) and for **DBAF-N$_2$**, the reflex at 9.75 Å to the (10$\bar{1}$) plane (9.77 Å calculated from the signal crystal data). Both molecules show an edge-on orientation and a layered structure. **DBAF** stays more tilted (43°–44°) than **DBAF-N$_2$** (77°–78°) to the substrate, which could slightly lower the HOMO level. Within one layer, both **DBAF** and **DBAF-N$_2$** molecules stack in lines. The small π–π distance (**DBAF** 3.3 Å and **DBAF-N$_2$** 3.4 Å) of two adjacent molecules and a reasonable overlap of their electron clouds (~1/3 for **DBAF** and ~2/3 for **DBAF-N$_2$**) favor the horizontal charge-carrier hopping along the stack-propagating direction (Fig. 7b). This agrees with the values of the calculated transfer integrals (for **DBAF** $t_{\parallel,h}$ = 20 ± 14 meV and for **DBAF-N$_2$** $t_{\parallel,h}$ = 70 ± 24 meV). The main difference is found in the vertical perspective (parallel to the substrate surface normal) between the adjacent layers. **DBAF** shows an edge-to-face π–π-arrangement ($t_{\perp,h}$ = 1 ± 3 meV), whereas **DBAF-N$_2$** has an edge-to-edge arrangement, giving rise to a negligible overlap of the π-electron cloud of molecules stemming from different layers (Fig. 7i). Thus, the vertical charge-carrier transport in the **DBAF-N$_2$** thin-films is inefficient, leading to a larger contact resistance and thereby to a smaller effective charge-carrier mobility[54] compared to the **DBAF** TFTs. Another explanation for the substantial difference in measured charge-carrier mobilities is that unlike **DBAF**, **DBAF-N$_2$** does not form a completely closed film on the substrate surface (as indicated by the AFM images in the ESI in Fig. S74‡), which is expected to greatly impede the lateral charge transport.
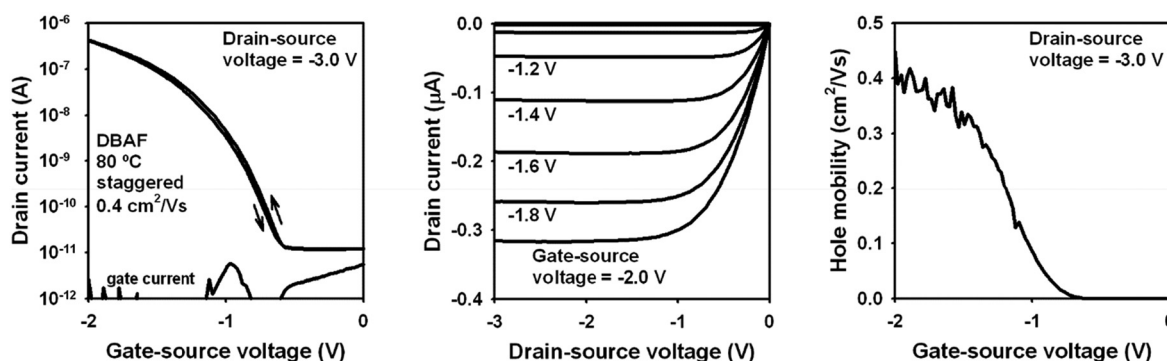
Fig. 6 Electrical characteristics of a **DBAF** TFT fabricated on a flexible PEN substrate in the inverted staggered (bottom-gate, top-contact) device architecture using an *n*-tetradecylphosphonic acid SAM as part of the gate dielectric, with the substrate held at a temperature of 80 °C during the semiconductor deposition. The effective charge-carrier mobility is 0.4 cm^2 V^{-1} s^{-1}.

This journal is © the Partner Organisations 2024

Org. Chem. Front., 2024, **11**, 5340–5349 | **5345**
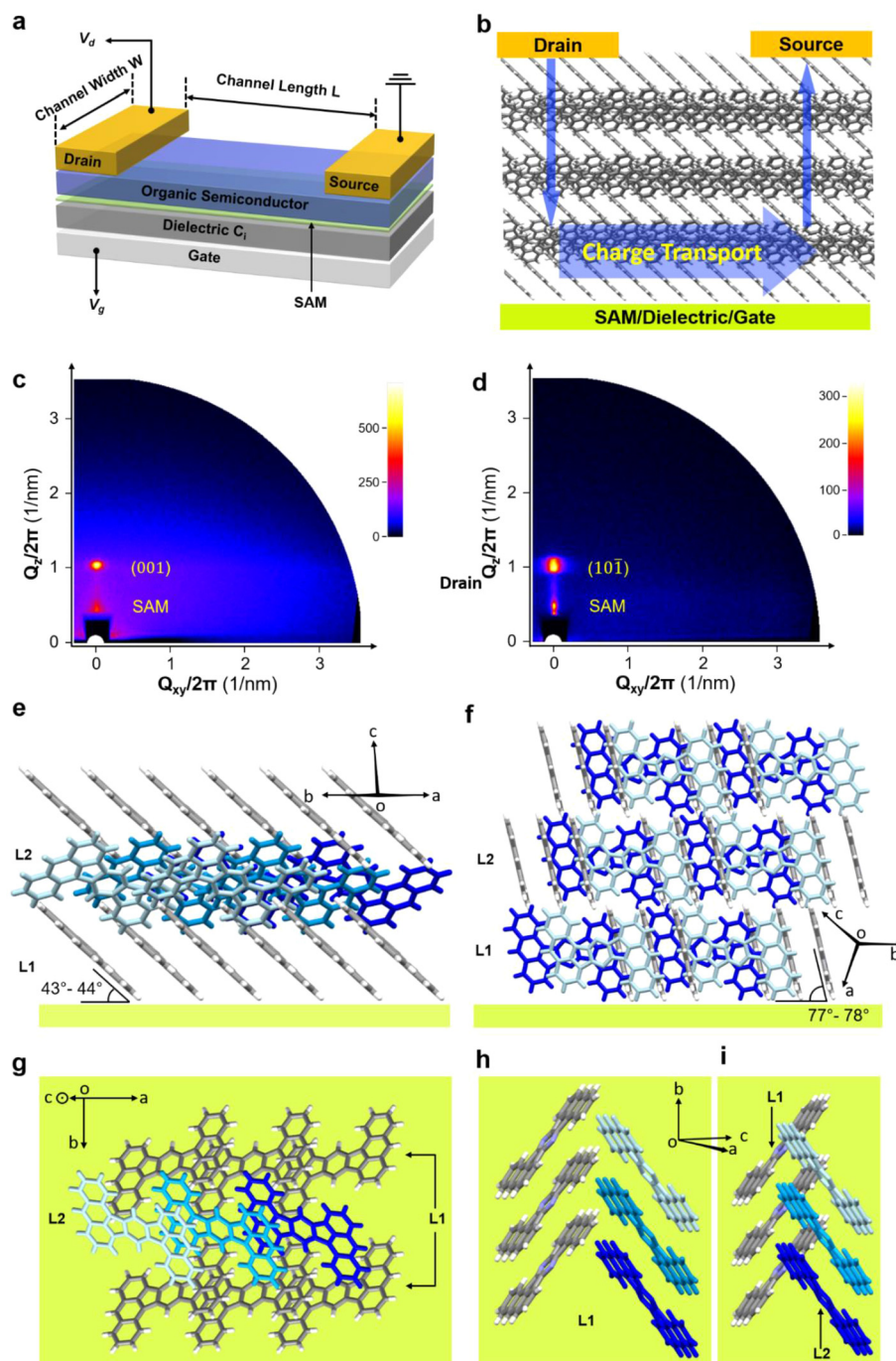
Fig. 7 Molecular orientation of **DBAF** and **DBAF-N$_2$** at the organic/SAM/inorganic interface of the OTFT devices. (a) The OTFT device used in this work has a bottom-gate-top-contact structure. (b) Illustration of charge transport taking place in a working device of **DBAF**. (c) and (d) are typical GIWAXS data for the **DBAF**- and **DBAF-N$_2$**-based devices, respectively. (e) Side view and (g) top view of the orientation of **DBAF** molecules. (f) Side view and (h and i) top views of the orientation of **DBAF-N$_2$** molecules. (h) shows the first layer (L1) at the SAM/inorganic substrate (bright green). (g) and (i) show the first two layers, in which molecules colored in grey come from the first layer (L1) and molecules in various blue colors are from the second layer (L2).

Conclusions

The PAHs presented in this study have a Z-shape conformation and can be tuned in terms of their solubility by peripheral substituents without influencing the electronic properties of the core structure as proven by spectroscopic methods and quantum chemical calculations. This made the investigation in solution as *e.g.* by electrochemical methods possible and revealed suitable characteristics for the application in p-type thin-film transistors. Corresponding devices of **DBAF** showed

5346 | *Org. Chem. Front.*, 2024, **11**, 5340–5349

This journal is © the Partner Organisations 2024

experimental mobilities up to $\mu_{h,exp} = 0.4$ cm^2 V^{-1} s^{-1} which is in agreement to quantum chemical calculations based on single crystal X-ray structure data. A substitution of two carbon atoms in the aromatic backbone with nitrogen was possible by simple modification of the molecular precursors. While an expected stabilization of the frontier molecular orbitals was achieved and higher theoretical hole mobilities were obtained, proving the beneficial intrinsic properties of **DBAF-N$_2$**, the corresponding devices suffered from a disadvantageous orientation of the crystalline films on the devices' surface resulting in three orders of magnitude smaller experimental mobilities. This study shows on the one hand the potential of this class of PAHs for the application as semiconducting materials in organic electronics and on the other hand the importance of the interplay of suitable intrinsic molecular properties and the controllable device morphology upon structural changes on a molecular level.

Data availability

The data that support the findings of this study are available from the corresponding author upon reasonable request.

Conflicts of interest

There are no conflicts to declare.

Acknowledgements

References

1 R. Zahradník, Electronic Structure and Properties of Non-Alternant Hydrocarbons, *Angew. Chem., Int. Ed. Engl.*, 1965, **4**, 1039–1050.

2 K. N. Plunkett, What About the Five-Membered Ring? Cyclopenta-fused Polycyclic Aromatic Hydrocarbons as a Building Block for Functional Materials, *Synlett*, 2013, **24**, 898–902.

3 R. G. Lawton and W. E. Barth, Synthesis of corannulene, *J. Am. Chem. Soc.*, 1971, **93**, 1730–1745.

4 A. M. Butterfield, B. Gilomen and J. S. Siegel, Kilogram-Scale Production of Corannulene, *Org. Process Res. Dev.*, 2012, **16**, 664–676.

5 X. Li, F. Kang and M. Inagaki, Buckybowls: Corannulene and Its Derivatives, *Small*, 2016, **12**, 3206–3223.

6 J. D. Wood, J. L. Jellison, A. D. Finke, L. Wang and K. N. Plunkett, Electron Acceptors Based on Functionalizable Cyclopenta[hi]aceanthrylenes and Dicyclopenta[de,mn]tetracenes, *J. Am. Chem. Soc.*, 2012, **134**, 15783–15789.

7 G. C. Kulkarni, J. L. Morales-Cruz, W. A. Hussain, I. J. Garvey and K. N. Plunkett, Electron Acceptors Based on Cyclopentannulated Tetracenes, *Synlett*, 2018, **29**, 2572–2576.

8 E. Misselwitz, J. Spengler, F. Rominger and M. Kivala, Indenoannulated Tridecacyclene: An All-Carbon Seven-Stage Redox-Amphoter, *Chem. – Eur. J.*, 2024, **30**, e202400696.

9 S. M. Elbert, A. Haidisch, T. Kirschbaum, F. Rominger, U. Zschieschang, H. Klauk and M. Mastalerz, 2,7,11,16-Tetra-tert-Butyl Tetraindenopyrene Revisited by an "Inverse" Synthetic Approach, *Chem. – Eur. J.*, 2020, **26**, 10585–10590.

10 H. Tanoguchi, T. Yuki, S. Yokokura, T. Yanase, M. Jin, H. Ito, T. Nagahama and T. Shimada, Single Crystal Growth of Cyclopenta-Fused Polycyclic Aromatic Hydrocarbon by the Naphthalene Flux Method: 2D Ambipolar Charge Transport Properties and NIR Absorption, *ACS Appl. Electron. Mater.*, 2023, **5**, 6266–6274.

11 A. Naibi Lakshminarayana, J. Chang, J. Luo, B. Zheng, K.-W. Huang and C. Chi, Bisindeno-annulated pentacenes with exceptionally high photo-stability and ordered molecular packing: simple synthesis by a regio-selective Scholl reaction, *Chem. Commun.*, 2015, **51**, 3604–3607.

12 H.-H. Hseuh, M.-Y. Hsu, T.-L. Wu and R.-S. Liu, Efficient Synthesis and Characterization of Dibenzo[a,m]rubicenes and Tetrabenzo[a,f,r,m]rubicenes, *J. Org. Chem.*, 2009, **74**, 8448–8451.

13 X. Gu, X. Xu, H. Li, Z. Liu and Q. Miao, Synthesis, Molecular Packing, and Thin Film Transistors of Dibenzo[a,m]rubicenes, *J. Am. Chem. Soc.*, 2015, **137**, 16203–16208.

14 L. Ma, Y. Han, Q. Shi and H. Huang, The design, synthesis and application of rubicene based polycyclic aromatic hydrocarbons (PAHs), *J. Mater. Chem. C*, 2023, **11**, 16429–16438.

15 H. Sakurai, T. Daiko and T. Hirao, A Synthesis of Sumanene, a Fullerene Fragment, *Science*, 2003, **301**, 1878–1878.

16 S. H. Tucker, Synthesis of fluoranthenes. Part XIII. Synthesis of benzo[1:2-a, 3:4-a′]- and of benzo[1:2-a, 4:5-a′]-diacenaphthylene, *J. Chem. Soc.*, 1958, 1462–1465.

17 L. Han, K. Ye, C. Li, Y. Zhang, H. Zhang and Y. Wang, Thermally Stable and Highly Luminescent Green Emissive Fluorophores with Acenaphtho[1,2-k]fluoranthene Cores and Aromatic Amine Groups, *ChemPlusChem*, 2017, **82**, 315–322.

18 Y.-C. Hsieh, H.-Y. Fang, Y.-T. Chen, R. Yang, C.-I. Yang, P.-T. Chou, M.-Y. Kuo and Y.-T. Wu, Zethrene and

This journal is © the Partner Organisations 2024

Org. Chem. Front., 2024, **11**, 5340–5349 | **5347**

Dibenzozethrene: Masked Biradical Molecules?, *Angew. Chem., Int. Ed.*, 2015, **54**, 3069–3073.

19 L. Shan, Z. Liang, X. Xu, Q. Tang and Q. Miao, Revisiting zethrene: synthesis, reactivity and semiconductor properties, *Chem. Sci.*, 2013, **4**, 3294–3297.

20 Z. Sun, S. Lee, K. H. Park, X. Zhu, W. Zhang, B. Zheng, P. Hu, Z. Zeng, S. Das, Y. Li, C. Chi, R.-W. Li, K.-W. Huang, J. Ding, D. Kim and J. Wu, Dibenzoheptazethrene Isomers with Different Biradical Characters: An Exercise of Clar's Aromatic Sextet Rule in Singlet Biradicaloids, *J. Am. Chem. Soc.*, 2013, **135**, 18229–18236.

21 C. Zong, X. Zhu, Z. Xu, L. Zhang, J. Xu, J. Guo, Q. Xiang, Z. Zeng, W. Hu, J. Wu, R. Li and Z. Sun, Isomeric Dibenzoheptazethrenes for Air-Stable Organic Field-Effect Transistors, *Angew. Chem., Int. Ed.*, 2021, **60**, 16230–16236.

22 R. Fittig and E. Ostermayer, Ueber das Phenanthren, einen neuen Kohlenwasserstoff im Steinkohlentheer, *Liebigs Ann. Chem.*, 1873, **166**, 361–382.

23 A. Schmitz and I. Ueber, hochsiedende Kohlenwasserstoffe des Steinkohlentheers, *Liebigs Ann. Chem.*, 1878, **193**, 115–128.

24 V. Sachweh and H. Langhals, Synthese von Reinst-Rubicen und Rubicen-Derivaten, *Chem. Ber.*, 1990, **123**, 1981–1987.

25 M. Kawamura, E. Tsurumaki and S. Toyota, Facile Synthesis of Rubicenes by Scholl Reaction, *Synthesis*, 2018, 134–138.

26 S. Toyota, S. Ban, M. Hara, M. Kawamura, H. Ikeda and E. Tsurumaki, Synthesis and Properties of Rubicene-Based Aromatic π-Conjugated Compounds as Five-Membered Ring Embedded Planar Nanographenes, *Chem. – Eur. J.*, 2023, **29**, e202301346.

27 C. H. E. Chow, Y. Han, H. Phan and J. Wu, Nitrogen-doped Heptazethrene and Octazethrene Diradicaloids, *Chem. Commun.*, 2019, **55**, 9100–9103.

28 K. Fujimoto, S. Takimoto, S. Masuda, T. Inuzuka, K. Sanada, M. Sakamoto and M. Takahashi, 5,11-Diazadibenzo[hi,qr]tetracene: Synthesis, Properties, and Reactivity toward Nucleophilic Reagents, *Chem. – Eur. J.*, 2021, **27**, 8951–8955.

29 K. Tajima, K. Matsuo, H. Yamada, N. Fukui and H. Shinokubo, Diazazethrene bisimide: a strongly electron-accepting π-system synthesized via the incorporation of both imide substituents and imine-type nitrogen atoms into zethrene, *Chem. Sci.*, 2023, **14**, 635–642.

30 Y. S. Park, D. J. Dibble, J. Kim, R. C. Lopez, E. Vargas and A. A. Gorodetsky, Synthesis of Nitrogen-Containing Rubicene and Tetrabenzopentacene Derivatives, *Angew. Chem., Int. Ed.*, 2016, **55**, 3352–3355.

31 Y. Morimoto, Y. H. Koo, K. Otsubo, H. Kitakado, S. Seki, A. Osuka and T. Tanaka, Dibenzodiazapyracylenes: Doubly N-Doped Cyclopenta-Fused Polycyclic Molecules That Exhibit High Carrier Mobility, *Angew. Chem., Int. Ed.*, 2022, **61**, e202200341.

32 H. W. H. Lai, Y. C. Teo and Y. Xia, Functionalized Rigid Ladder Polymers from Catalytic Arene-Norbornene

33 P. Meti, E.-S. Lee, J.-W. Yang and Y.-D. Gong, Regioselective synthesis of dipyrrolopyrazine (DPP) derivatives via metal free and metal catalyzed amination and investigation of their optical and thermal properties, *RSC Adv.*, 2017, **7**, 18120–18131.

34 B. D. Steinberg, E. A. Jackson, A. S. Filatov, A. Wakamiya, M. A. Petrukhina and L. T. Scott, Aromatic π-Systems More Curved Than C60. The Complete Family of All Indenocorannulenes Synthesized by Iterative Microwave-Assisted Intramolecular Arylations, *J. Am. Chem. Soc.*, 2009, **131**, 10537–10545.

35 M.-K. Chen, H.-J. Hsin, T.-C. Wu, B.-Y. Kang, Y.-W. Lee, M.-Y. Kuo and Y.-T. Wu, Highly Curved Bowl-Shaped Fragments of Fullerenes: Synthesis, Structural Analysis, and Physical Properties, *Chem. – Eur. J.*, 2014, **20**, 598–608.

36 T. Kubo, S. Miyazaki, T. Kodama, M. Aoba, Y. Hirao and H. Kurata, A facile synthesis of trinaphtho[3.3.3]propellane and its π-extension and the formation of a two-dimensional honeycomb molecular assembly, *Chem. Commun.*, 2015, **51**, 3801–3803.

37 Y.-C. Hsieh, T.-C. Wu, J.-Y. Li, Y.-T. Chen, M.-Y. Kuo, P.-T. Chou and Y.-T. Wu, Dinaphthozethrene and Diindenozethrene: Synthesis, Structural Analysis, and Properties, *Org. Lett.*, 2016, **18**, 1868–1871.

38 X. Tian, L. M. Roch, K. K. Baldridge and J. S. Siegel, Diindenocorannulenes: Curved Aromatics Blending Bowl-in-Bowl Assembly and Nanocarbon Material Properties, *Eur. J. Org. Chem.*, 2017, 2801–2805.

39 Y. Wang, O. Allemann, T. S. Balaban, N. Vanthuyne, A. Linden, K. K. Baldridge and J. S. Siegel, Chiral Atropisomeric Indenocorannulene Bowls: Critique of the Cahn–Ingold–Prelog Conception of Molecular Chirality, *Angew. Chem., Int. Ed.*, 2018, **57**, 6470–6474.

40 S. Seifert, D. Schmidt, K. Shoyama and F. Würthner, Base-Selective Five- versus Six-Membered Ring Annulation in Palladium-Catalyzed C–C Coupling Cascade Reactions: New Access to Electron-Poor Polycyclic Aromatic Dicarboximides, *Angew. Chem., Int. Ed.*, 2017, **56**, 7595–7600.

41 X.-Y. Wang, X. Yao and K. Müllen, Polycyclic aromatic hydrocarbons in the graphene era, *Sci. China: Chem.*, 2019, **62**, 1099–1144.

42 U. H. F. Bunz and J. Freudenberg, N-Heteroacenes and N-Heteroarenes as N-Nanocarbon Segments, *Acc. Chem. Res.*, 2019, **52**, 1575–1587.

43 T. Kirschbaum, F. Rominger and M. Mastalerz, A Chiral Polycyclic Aromatic Hydrocarbon Monkey Saddle, *Angew. Chem., Int. Ed.*, 2020, **59**, 270–274.

44 T. Kirschbaum, F. Rominger and M. Mastalerz, An Isosteric Triaza Analogue of a Polycyclic Aromatic Hydrocarbon Monkey Saddle, *Chem. – Eur. J.*, 2020, **26**, 14560–14564.

45 X. Roy, J. H. Chong, B. O. Patrick and M. J. MacLachlan, Molecular Scaffolding of Prussian Blue Analogues Using a

Annulation Polymerization, *ACS Macro Lett.*, 2017, **6**, 1357–1361.

5348 | *Org. Chem. Front.*, 2024, **11**, 5340–5349

This journal is © the Partner Organisations 2024

Phenanthroline-Extended Triptycene Ligand, *Cryst. Growth Des.*, 2011, **11**, 4551–4558.

46 L. Ueberricke, J. Schwarz, F. Ghalami, M. Matthiesen, F. Rominger, S. M. Elbert, J. Zaumseil, M. Elstner and M. Mastalerz, Triptycene End-Capped Benzothieno-benzothiophene and Naphthothienobenzothiophene, *Chem. – Eur. J.*, 2020, **26**, 12596–12605.

47 L. Ueberricke, I. Ciubotaru, F. Ghalami, F. Mildner, F. Rominger, M. Elstner and M. Mastalerz, Di- and Tetracyano-Substituted Pyrene-Fused Pyrazaacenes: Aggregation in the Solid State, *Chem. – Eur. J.*, 2020, **26**, 11634–11642.

48 S. Roosta, F. Ghalami, M. Elstner and W. Xie, Efficient Surface Hopping Approach for Modeling Charge Transport in Organic Semiconductors, *J. Chem. Theory Comput.*, 2022, **18**, 1264–1274.

49 W. Xie, D. Holub, T. Kubař and M. Elstner, Performance of Mixed Quantum-Classical Approaches on Modeling the Crossover from Hopping to Bandlike Charge Transport in Organic Semiconductors, *J. Chem. Theory Comput.*, 2020, **16**, 2071–2084.

50 H. Klauk, Organic thin-film transistors, *Chem. Soc. Rev.*, 2010, **39**, 2643–2666.

51 A. Heck, J. J. Kranz, T. Kubař and M. Elstner, Multi-Scale Approach to Non-Adiabatic Charge Transport in High-Mobility Organic Semiconductors, *J. Chem. Theory Comput.*, 2015, **11**, 5068–5082.

52 U. Kraft, U. Zschieschang, F. Ante, D. Kälblein, C. Kamella, K. Amsharov, M. Jansen, K. Kern, E. Weber and H. Klauk, Fluoroalkylphosphonic acid self-assembled monolayer gate dielectrics for threshold-voltage control in low-voltage organic thin-film transistors, *J. Mater. Chem.*, 2010, **20**, 6416–6418.

53 M. Birkholz, in *Thin Film Analysis by X-Ray Scattering*, WILEY-VCH Verlag GmbH & Co. KGaA, 2006.

54 B. Peng, K. Cao, A. H. Y. Lau, M. Chen, Y. Lu and P. K. L. Chan, Crystallized Monolayer Semiconductor for Ohmic Contact Resistance, High Intrinsic Gain, and High Current Density, *Adv. Mater.*, 2020, **32**, 2002281.

This journal is © the Partner Organisations 2024

Org. Chem. Front., 2024, **11**, 5340–5349 | **5349**